Article

Cell Reports

Widespread Accumulation of Ribosome-Associated Isolated 3′ UTRs in Neuronal Cell Populations of the Aging Brain

Graphical Abstract

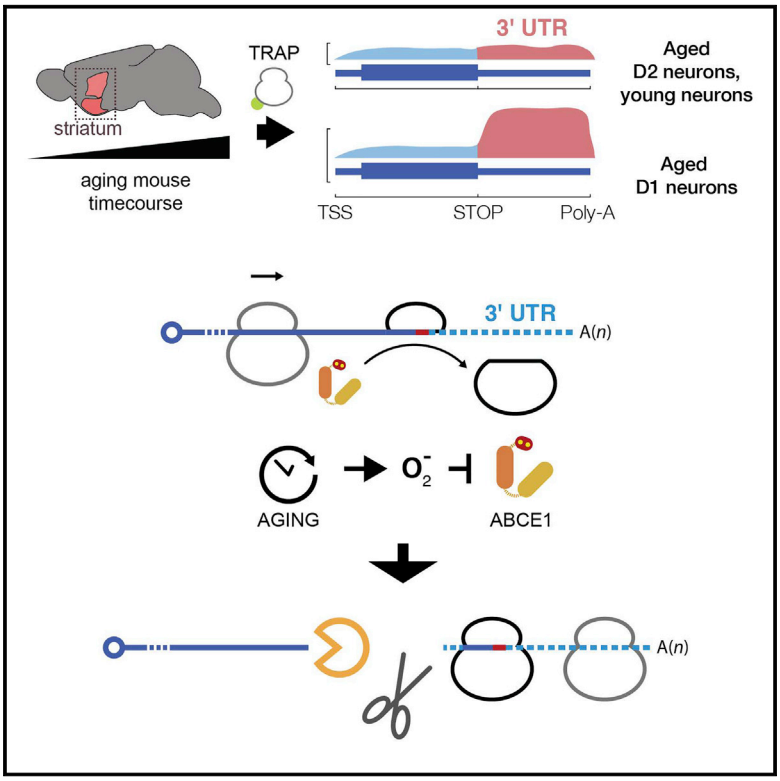

Highlights

- Isolated 3′ UTRs accumulate in aging D1 spiny projection neurons of mouse striatum
- 3′ UTR RNAs occur with oxidative stress and can be induced by ROS-inducing drugs
- 3′ UTR RNAs are associated with the aging human brain and short peptide production
- Isolated 3′ UTRs may result from impaired ABCE1 and deficient ribosome recycling

Authors

Peter H. Sudmant, Hyeseung Lee, Daniel Dominguez, Myriam Heiman, Christopher B. Burge

Correspondence

mheiman@mit.edu (M.H.), cburge@mit.edu (C.B.B.)

In Brief

Particular brain regions and cell populations exhibit increased susceptibility to aging-related stresses. Sudmant et al. report that fragments of mRNAs accumulate in the aging brains of mice and humans. These species are associated with ribosomes and the production of small peptides and reflect regional differences in metabolism and oxidative stress.

Sudmant et al., 2018, Cell Reports *25*, 2447–2456
November 27, 2018
https://doi.org/10.1016/j.celrep.2018.10.094

CellPress

Cell Reports
Article

Widespread Accumulation of Ribosome-Associated Isolated 3′ UTRs in Neuronal Cell Populations of the Aging Brain

Peter H. Sudmant,[1] Hyeseung Lee,[2] Daniel Dominguez,[1] Myriam Heiman,[2,*] and Christopher B. Burge[1,3,*]
[1]Department of Biology, Massachusetts Institute of Technology, 77 Massachusetts Ave., Cambridge, MA 02139, USA
[2]Picower Institute for Learning and Memory, Massachusetts Institute of Technology, 77 Massachusetts Ave., Cambridge, MA 02139, USA
[3]Lead Contact
*Correspondence: mheiman@mit.edu (M.H.), cburge@mit.edu (C.B.B.)
https://doi.org/10.1016/j.celrep.2018.10.094

SUMMARY

Particular brain regions and cell populations exhibit increased susceptibility to aging-related stresses. Here, we describe the age-specific and brain-region-specific accumulation of ribosome-associated 3′ UTR RNAs that lack the 5′ UTR and open reading frame. Our study reveals that this phenomenon impacts hundreds of genes in aged D1 spiny projection neurons of the mouse striatum and also occurs in the aging human brain. Isolated 3′ UTR accumulation is tightly correlated with mitochondrial gene expression and oxidative stress, with full-length mRNA expression that is reduced but not eliminated, and with production of short 3′ UTR-encoded peptides. Depletion of the oxidation-sensitive Fe-S cluster ribosome recycling factor ABCE1 induces the accumulation of 3′ UTRs, consistent with a model in which ribosome stalling and mRNA cleavage by No-Go decay yields isolated 3′ UTR RNAs protected by ribosomes. Isolated 3′ UTR accumulation is a hallmark of brain aging, likely reflecting regional differences in metabolism and oxidative stress.

INTRODUCTION

Aging is characterized by impaired molecular function and the progressive accumulation of cellular damage (López-Otín et al., 2013). In the human brain, these processes—in combination with genetic and environmental factors—can result in neurodegenerative conditions, such as Alzheimer's disease and a general decline in memory and cognitive ability. Neurodegenerative diseases tend to impact specific cell populations and regions of the aging brain—a phenomenon known as selective neuronal vulnerability (Mattson and Magnus, 2006)—but why particular cells and brain regions exhibit increased susceptibility to the stresses of aging and the underlying molecular mechanisms are not well understood.

Recently, *in situ* hybridization has provided support for the existence of a class of RNAs in mouse neurons consisting exclusively of the 3′ UTRs of mRNAs absent the open reading frame (ORF) or 5′ UTR (Kocabas et al., 2015). Several isolated 3′ UTR species tested showed differential spatial and temporal distribution during development, and two were linked with reductions in the overall level of protein produced from the associated gene. Several other studies have also reported the phenomenon of isolated 3′ UTRs. A study of data from mammalian capped analysis of gene expression (CAGE) sequencing concluded that these species were likely the result of post-transcriptional cleavage (Mercer et al., 2011). Other studies have also concluded that CAGE sequencing captures some cleavage products, including a class of 3′ UTR species that exhibit both conservation and an enriched 5′ GGG sequence (Carninci et al., 2006; Fejes-Toth et al., 2009). CAGE-detected cleavage products originating in 3′ UTRs also showed substantial overlap (40%) with Ago2- and Drosha-independent cleavage products identified from transcriptome-wide profiling of endonucleolytic cleavage products that retain a 5′ phosphate (Karginov et al., 2010). Isolated 3′ UTRs have also been described in murine immune cells and human cell lines (Malka et al., 2017). However, the biogenesis and potential functions of isolated 3′ UTRs, and whether they are of particular importance in the brain are not well understood.

Here, we characterize the distribution of isolated 3′ UTRs throughout the aging mouse and human brain, demonstrating their widespread accumulation as a function of age. We observe that these RNAs vary substantially in abundance between different cell types and regions and are associated with signatures of oxidative stress. We provide evidence for a model of isolated 3′ UTR biogenesis in which oxidative stress impairs translation termination, triggering the entry of ribosomes into the 3′ UTR and endonucleolytic cleavage of mRNAs near the stop codon by the No-Go decay pathway.

RESULTS

Isolated 3′ UTRs Accumulate in Specific Aged Neuronal Cell Types of the Mouse Striatum

The striatum is impacted in both Huntington's disease and Parkinson's disease, both age-dependent neurodegenerative conditions. To identify cell-type-specific and age-associated changes in translating mRNAs that might contribute to age-associated degeneration of striatal neurons, we profiled ribosome-associated mRNAs from the two major neuronal cell subtypes of this region: spiny projection neurons (SPNs) of the direct and

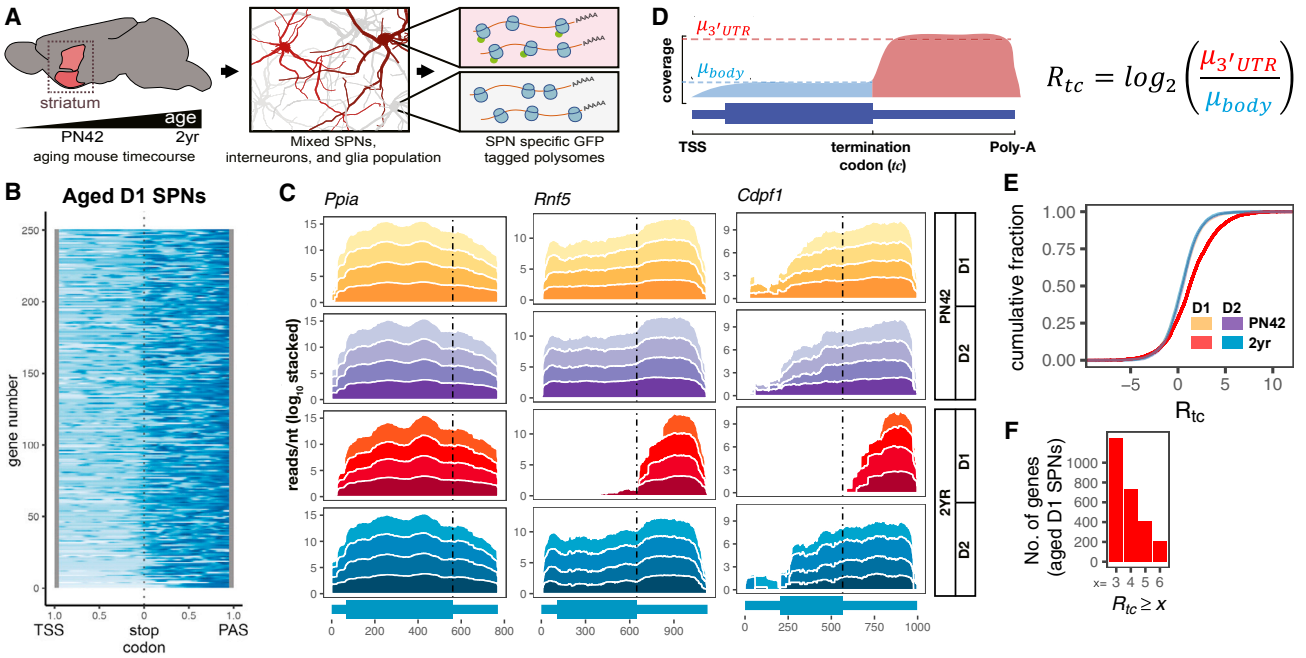

Figure 1. Isolated 3′ UTRs Accumulate in Aged D1 SPNs of the Mouse Striatum, but Not D2 SPNs or Young SPNs

(A) Overview of the TRAP protocol used to isolate cell-type-specific mRNA from D1 and D2 SPNs of the mouse striatum in young and aged mice.

(B) Heatmap of normalized read coverage over the 250 most 3′ UTR-enriched genes (see below) in 2-year-old D1 SPNs centered on the stop codon and extending 5′ and 3′ to the TSS and poly(A) site, respectively.

(C) Examples of the $\log_{10}$ coverage of four biological replicates per condition stacked on top of each other across a control gene, *Ppia,* and two genes exhibiting isolated 3′ UTRs exclusively in aged D1 SPNs. Dotted line indicates the stop codon.

(D) Schematic of the R_{tc} metric.

(E) The cumulative distribution of R_{tc} values of genes among the mouse SPN samples reveals a long tail for aged D1 SPNs.

(F) Counts of the number of genes at various R_{tc} cutoffs in aged D1 SPNs.

indirect pathways—referred to hereafter as D1 and D2 SPNs, respectively. Cell-type-specific translating mRNAs were isolated in young and aged mice by using translating ribosome affinity purification (TRAP), which makes use of transgenic mouse lines expressing an EGFP-tagged L10a ribosomal protein gene driven by a cell-type-specific promoter (Heiman et al., 2008). D1 and D2 SPNs express almost exclusively *Drd1a* or *Drd2* (dopamine receptors 1 and 2), respectively, the regulatory elements of which were used to drive expression of the tagged L10a protein. This system thus allows for cell-type-specific isolation of ribosome-associated mRNA from each of these cell types, avoiding contamination from non-neuronal cell types (Figure 1A).

TRAP RNA was isolated in biological quadruplicate from 42-day-old (PN42) and 2-year-old D1- and D2-tagged mice, and ribosome-associated (non-poly(A)-selected, rRNA depleted) RNA was sequenced. This sequencing procedure captures all ribosome-associated RNAs, including those without a poly(A) tail in a highly specific fashion (Figure S1A). In addition to gene expression changes across thousands of genes (see below), a meta-gene analysis of sequencing coverage profiles aligned to the stop codon indicated a dramatic increase in sequence reads at and beyond the stop codon in aged D1 SPNs (Figures 1B and S1B). This pattern was not observed in aged D2 SPNs or in samples from young mice (Figure 1C). An inspection of read coverage profiles identified a subset of genes in aged D1 SPNs that had read coverage exclusively or mostly restricted to the 3′ UTR. This pattern was highly consistent across biological replicates (Figure S1C). We confirmed a several-fold increased abundance of 3′ UTRs relative to coding regions in aged D1 SPNs for several of these genes by qPCR analysis (Figure S1D), suggesting that full-length (or ORF-only) mRNAs are reduced but not absent for this set of genes. The signatures associated with isolated 3′ UTRs observed here in aged D1 SPNs are of much greater magnitude and extend across far more genes than has been previously reported (Kocabas et al., 2015; Malka et al., 2017).

To quantify the extent of 3′ UTR enrichment of a gene in a dataset, we developed a simple metric that we call the "termination codon ratio," R_{tc}, defined as the $\log_2$ of the ratio of read density in the 3′ UTR of a gene to read density in the body of the gene (including coding region and 5′ UTR, STAR Methods), restricted to constitutive portions of the gene (Figure 1D). R_{tc} is analogous to measures used previously to quantify ribosome occupancy in 3′ UTRs from ribosome footprint data (Mills et al., 2016), but when applied to TRAP or RNA-seq data, R_{tc} measures the positional enrichment of transcript fragments rather than ribosome abundance. The distribution of R_{tc} values was approximately symmetrical, with a mean slightly above 0 across young D1 SPNs (mean R_{tc} = 0.44) and aged D2 SPNs (mean R_{tc} = 0.38), but was substantially skewed toward larger values in aged D1 SPNs (mean R_{tc} = 1.34, $p < 2.2e{-}16$, Wilcoxon

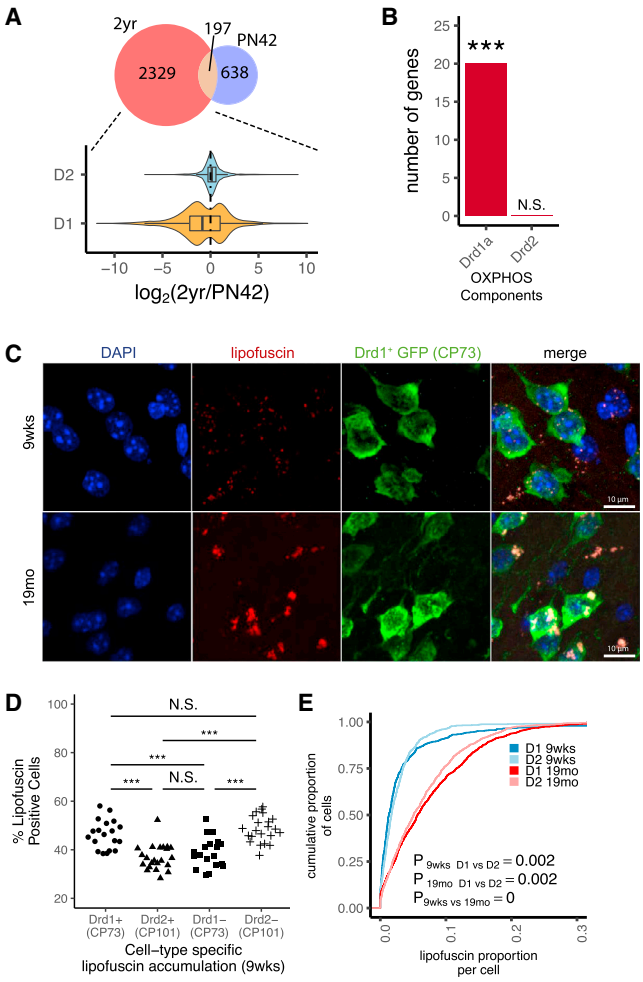

Figure 2. Increased Levels of Oxidative Stress Accompany Isolated 3′ UTR Accumulation in Aging D1 SPNs

(A) Venn diagram depicting the number of genes differentially expressed between D1 and D2 SPNs at each time point and the log-fold intra-cell-type gene expression changes from PN42 to 2 years.

(B) The number of core components of oxidative phosphorylation differentially expressed between young and old D1 and D2 SPNs. p values indicate enrichment over background. ***p < 0.001, hypergeometric test.

(C) Representative images of DAPI, lipofuscin, GFP, and merged channels for 9-week and 19-month-old CP73 mice expressing EGFP-L10a in D1 SPNs.

(D) The proportion of lipofuscin-positive cells in GFP ± cells in CP73 and CP101 mouse lines at 9 weeks. Each point represents a slide and the x-coordinate was jittered to improve readability. ***p < 0.001, chi-squared test.

(E) The cumulative distribution of the proportional area of each cell positive for lipofuscin accumulation in 9-week and 19-month-old mice.

rank-sum test; Figure 1E). Among aged D1 SPNs, 404 genes exhibited an $R_{tc} \geq 5$, indicating at least 2^5 = 32-fold enrichment of reads in 3′ UTR relative to gene body, versus 66 and 52 genes observed at this cutoff in young D1 SPNs and aged D2 SPNs, respectively (Figure 1F). Genes with increased R_{tc} represented a variety of functions and pathways (none strongly enriched) and were generally shorter, with a higher C+G content and an increased potential for 3′ UTR RNA secondary than expressed genes overall (Figures S1E and S1F).

Although the presence of 3′ UTR RNAs lacking the coding region has been observed previously in some instances (Carninci et al., 2006; Kocabas et al., 2015; Malka et al., 2017; Mercer et al., 2011), the mechanism of their biogenesis remains elusive. Analyzing total RNA sequencing data from several mouse tissues and the mouse NIH 3T3 cell line, we identified several genes, including *Frat2*, *Hnrnpa0*, and *Sox12*, that had read densities at least several-fold higher in the 3′ UTR than in the coding region in most or all of these samples (Figures S1G and S1H). Thus, the phenomenon of 3′ UTR-enriched genes observed so widely in aged D1 SPNs extends to some genes in other mouse cells and tissues, as observed previously (Kocabas et al., 2015; Malka et al., 2017).

Aged D1 SPNs Exhibit Increased Oxidative Damage Compared to D2 and Young SPNs

Because gene expression signatures can provide information about cellular environmental conditions, we examined gene expression profiles of young and aged mouse SPNs for clues to the conditions that give rise to 3′ UTR enrichment. Young D1 and D2 SPNs exhibited cell-type-specific expression signatures typical of those that have been observed previously by microarray and single-cell sequencing studies (Gokce et al., 2016; Heiman et al., 2008). However, 2-year-old mice exhibited three times as many differentially expressed genes as PN42 mice (2526 genes compared to 835; Figure 2A). Changes in expression levels between young and aged D1 SPNs, rather than changes in D2 SPNs, explained most of these differences, and a pathway analysis of genes differentially expressed between aged SPN subtypes showed an enrichment in nuclear-encoded oxidative phosphorylation (OXPHOS) components (Figures 2B and S2A–S2C). We also observed increased expression of the primary mitochondrial superoxide dismutase *Sod2*, which plays crucial roles in eliminating reactive oxygen species (ROS) and sensing oxidative phosphorylation-associated distress (Zou et al., 2017) and changes in other reactive oxygen response genes in aging D1 SPNs (Figure S2D). These observations raised the possibility that D1 SPNs might be exposed to higher levels of oxygen free radicals.

To ask whether D1 SPNs are exposed to higher levels of oxidative stress, we quantified lipofuscin aggregates, a byproduct of oxidatively damaged proteins, lipids, and mitochondria, in sectioned striata of both young and aged mouse lines expressing GFP in either a D1-specific (CP73) or D2-specific (CP101) manner (Figure 2C). Some 95% of the neuronal cells of the striatum are SPNs, allowing us to directly compare the accumulation of lipofuscin in GFP-positive versus GFP-negative neurons in each of these mouse lines. Both aged D1 and aged D2 SPNs exhibited a significantly higher average per cell lipofuscin fraction than young SPNs ($p < 1e{-}10$, chi-square test), consistent with previous observations of lipofuscin aggregate accumulation in aging neurons (Nandy, 1971). However, at 9 weeks, 47.5% of D1 SPNs were positive for lipofuscin speckles compared to 37.8% of D2 SPNs (Figure 2D; $p < 1e{-}10$, chi-square test). Furthermore, the mean per cell lipofuscin fraction was also significantly higher in aged D1 SPNs compared to D2 SPNs (Figure 2E; p = 0.002, Wilcoxon rank-sum test). These observations support the idea that wild-type D1 SPNs are subject to greater exposure to oxygen free radical species during aging than D2 SPNs.

A Model of Isolated 3′ UTR Formation from Impaired ABCE1 Activity and Cleavage by the No-Go Decay Pathway

The association of ribosomes with isolated 3′ UTRs, implied by their isolation via TRAP, and the location of the increase in 3′ UTR enrichment close to the stop codon are consistent with a cytoplasmic, translation-linked mechanism for biogenesis of isolated 3′ UTRs. We considered a number of translation-associated mechanisms involving the 3′ UTR as possible sources of isolated 3′ UTRs. For example, nonsense-mediated mRNA decay (NMD) targets mRNAs with premature termination codons and/or long 3′ UTRs for degradation (Garneau et al., 2007). However, we observed no strong relationship between 3′ UTR length and 3′ UTR enrichment (Figure S1F), and NMD is associated with prematurely terminating ribosomes rather than 3′ UTR-associated ribosomes. Alternatively, translational read-through (i.e., translation extending through the stop codon) would yield 3′ UTR-associated ribosomes. However, read-through by itself does not produce mRNA fragments. Recent studies in yeast and mammalian hematopoietic cells have observed the accumulation of ribosomes in 3′ UTRs following depletion of the yeast ribosome recycling factor *Rli1* (Young et al., 2015) and of its human homolog, *ABCE1* (Mills et al., 2016). Depletion of *ABCE1* leads to the increased accumulation of ribosomes on the stop codon and subsequent reinitiation of translation in the 3′ UTRs of a subset of genes (Guydosh and Green, 2014; Young et al., 2015); the extent of this phenomenon varies widely between genes for reasons that are not understood. The failure of ABCE1 to efficiently recycle ribosomes on particular mRNAs has been associated with increased rates of both read-through and reinitiation, although mechanistic details are lacking (Guydosh and Green, 2014; Mills et al., 2016; Young et al., 2015).

A model in which the formation of 3′ UTR RNA fragments results from impaired ABCE1 activity is also consistent with the observed association between oxidative stress and 3′ UTR enrichment. ABCE1 contains two iron-sulfur clusters that are essential for its activity and are acutely sensitive to oxygen free radicals (Alhebshi et al., 2012). Treatment with ROS-inducing compounds, such as paraquat (PQ), impairs ABCE1 iron-sulfur cofactor uptake, reducing its activity (Alhebshi et al., 2012). In yeast, age-induced mitochondrial dysfunction leads to impaired assembly of iron-sulfur clusters, which are synthesized in the mitochondrial matrix, and targeted mRNA decay of numerous iron-dependent genes, including *Rli1* (Puig et al., 2005; Veatch et al., 2009). The induction of oxidative stress with hydrogen peroxide in yeast also increases the proportion of 3′ UTR ribosomes, consistent with defects in ribosome recycling (Gerashchenko and Lobanov, 2012).

Transcripts that fail to undergo translation termination and have stalled ribosomes are normally degraded through the PELO/HBS1-dependent No-Go decay (NGD) pathway, which induces endonucleolytic cleavage of the message just upstream of the stalled ribosome (Doma and Parker, 2006; Tsuboi et al., 2012). Cleavage of the mRNA yields two fragments, with the 5′ fragment degraded 3′-to-5′ by the exosome and the 3′ fragment normally degraded 5′-to-3′ by XRN1 (Tsuboi et al., 2012). This process has also been implicated in mRNA degradation during NMD (Arribere and Fire, 2018). A similar process of ribosome-associated endonucleolytic cleavage just upstream of ribosomes termed "ribothrypsis" has recently been reported and could be considered a generalized form of NGD (Ibrahim et al., 2018).

We hypothesized that the consistent failure of ABCE1 to recycle a ribosome from the stop codon of an mRNA and from its 3′ NGD cleavage product could produce a relatively stable 3′ UTR RNA species. Such an RNA would be protected from exonucleases at its 5′ end by a persistently stalled ribosome (and perhaps secondarily stalled ribosomes upstream) and at its 3′ end by the poly(A) tail (Figure 3A). Inhibition of ABCE1 is known to increase the rates of read-through and reinitiation (Guydosh and Green, 2014; Mills et al., 2016; Young et al., 2015), potentially giving rise to secondary RNA species. Read-through or reinitiation involves ribosome movement into the 3′ UTR, potentially yielding partial 3′ UTR fragments protected at their 5′ ends by secondarily stalled ribosomes (Figure 3A).

Depletion of *ABCE1* Induces Cleavage-Associated Fragments and 3′ UTR Enrichment

To directly test our hypothesis that reduced ABCE1 activity can trigger 3′ UTR enrichment, we used small interfering RNAs (siRNAs) to knock down *Abce1* in cultured NIH 3T3 cells (Figures 3B and S3A) and performed qRT-PCR with primers to the *Nanos1* gene, which showed robustly increased 3′ UTR enrichment in aged D1 SPNs. This knockdown resulted in a ~50% increase in 3′ UTR enrichment of *Nanos1* after 3 days, assessed using primer pairs in the 3′ UTR versus pairs in the ORF. To test whether oxidative stress could inhibit ABCE1 and subsequently induce isolated 3′ UTRs, we treated 3T3 cells with the drug PQ, a potent inducer of ROS. Over a 5-day treatment time course with 100 μM PQ, ABCE1 protein levels decreased by ~4-fold (Figure S3B), possibly by limiting or chelating iron and inhibiting the assembly or stability of ABCE1 (Brumaghim et al., 2003), demonstrating impacts of oxidative stress on the ABCE1 protein. Furthermore, PQ-induced ABCE1 depletion was accompanied by the increased 3′ UTR enrichment of *Nanos1* (measured after 72 hr; Figure 3B). Thus, both direct depletion and indirect oxidative stress-induced inhibition of ABCE1 activity can induce 3′ UTR accumulation.

To test the above model, we performed ribosome profiling in *Abce1* knockdown cells ("siA") and under induced oxidative stress by using PQ as described above. Results were compared to control siRNA ("siC"). Both PQ and siA treatments reduced ABCE1 levels by >90% (Figures S3A and S3B). Ribosome-protected RNAs were isolated from these samples and sequenced using standard techniques targeting ribosome-protected RNA fragments 15–32 nt long (STAR Methods).

To identify bulk changes in ribosome positioning in response to our treatment conditions, we generated metagene plots of the density of ribosome footprint 5′ ends from fragments 27–31 nt long, corresponding to the width of a ribosome. These plots showed the expected 3-nt periodicity over transcripts, and metagene plots centered on the stop codon showed a higher density of stop codon stalled ribosomes after knockdown of *Abce1* (Figure S3C), as reported previously (Mills et al., 2016; Young et al., 2015). We also observed a substantial increase in the density of 3′ UTR ribosomes after *Abce1* knockdown and PQ treatment (Figure 3C).

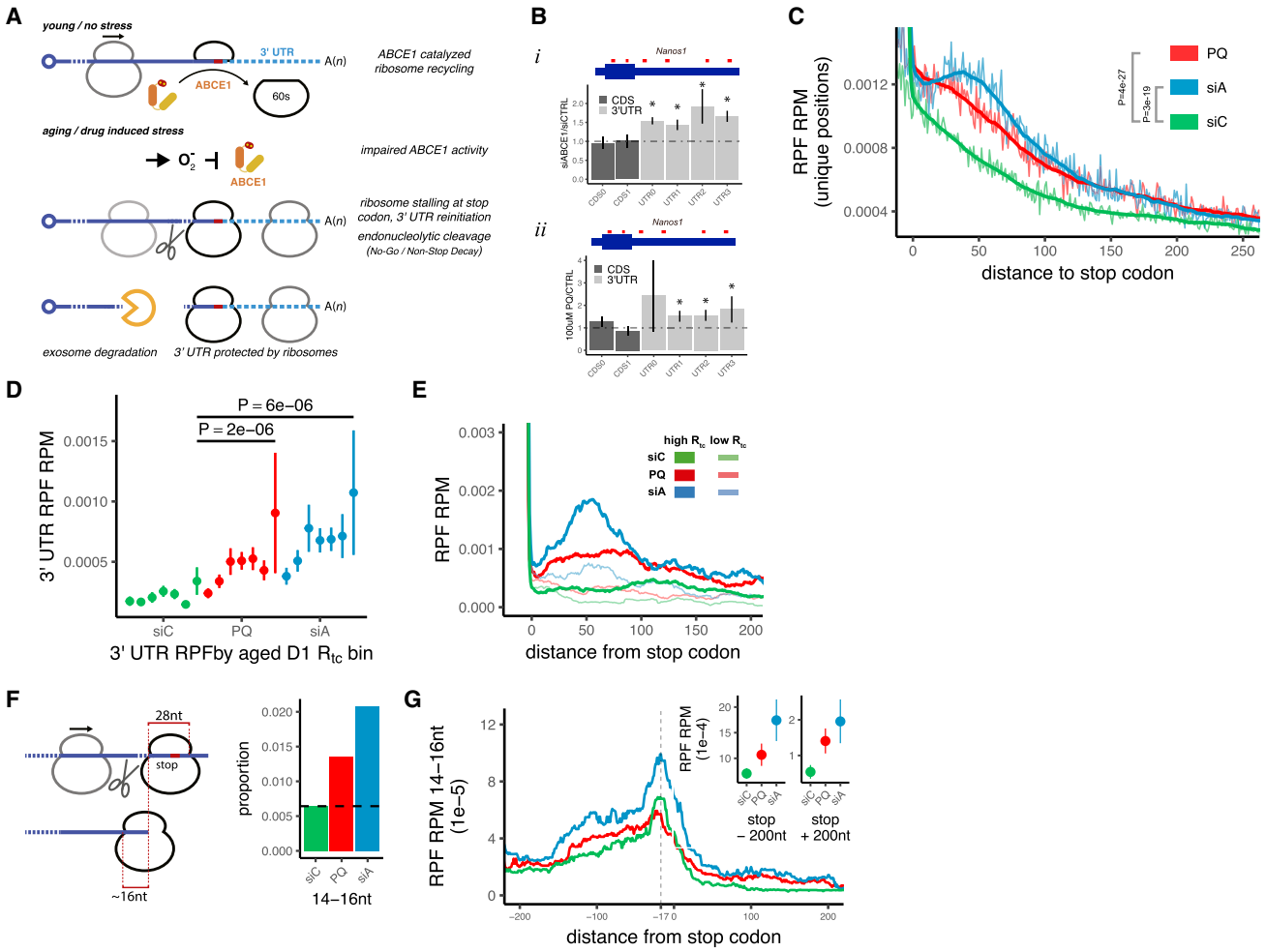

Figure 3. Oxidative Stress and ABCE1 Depletion Induce 3′ UTR Enrichment and a Model for Isolated 3′ UTR Accumulation

(A) A model of isolated 3′ UTR RNA species formation. An excess of age- or drug-induced ROS impairs the activity of the iron-sulfur cluster protein ribosome recycling factor ABCE1. ABCE1 deficiency results in an increase in ribosomes stalled on the stop codon and reinitiating in the 3′ UTR. Transcripts with stalled ribosomes are endonucleolytically cleaved upstream of stalled ribosomes by the No-Go decay pathway. The 5′ cleavage product is degraded by the 3′-to-5′ exosome, but the 3′ fragment is protected from Xrn1 5′-to-3′ digestion by stalled ribosome(s) at the stop codon.

(B) qPCR analysis of 3′ UTR abundance normalized to primer pairs in the coding region for *i*) cells treated for 3 days with siRNAs targeted to *Abce1* compared to cells transfected with control siRNAs and *ii*) cells treated for 3 days with 100 μM paraquat compared to untreated cells. Error bars indicate 95% confidence interval, * indicates significance by bootstrap ($p < 0.01$).

(C) Meta plot of the density (in average reads per million, RPM) of 5′ ends of 27- to 31-nt-long ribosome protected fragments (RPF) plotted as a function of distance from the stop codon. p values represent Wilcoxon Rank Sum test for the first 250 nt after the stop codon.

(D) Mean RPM +SEM in the 3′ UTRs of genes, binned by R_{tc} in aged D1 SPNs. p values represent the Wilcoxon Rank Sum test between the highest (7^{th}) bin of the control condition (siC) and the highest bin of each of the test conditions.

(E) Ribosome footprint density over the first 200 nt of the 3′ UTR from genes in the top and bottom 15% of aged D1 SPN R_{tc} values.

(F) Schematic of cleavage upstream of a stalled ribosome and subsequent protection of a short cleavage fragment by an upstream translating ribosome and the proportion of short cleavage fragments sequenced from each experimental condition.

(G) Smoothed meta plot of the density (in RPM) of short (14–16 nt) ribosome-protected fragments in relation to the stop codon for different experimental conditions. Insets are mean + SEM of RPM in the 200-nt upstream and downstream of the stop codon.

Our model of isolated 3′ UTR formation predicts that siABCE1 (small interfering RNA to ABCE1) or PQ treatment should induce 3′ UTR ribosomes specifically in genes susceptible to 3′ UTR enrichment compared to other genes. To test this hypothesis, we compared the density of 3′ UTR ribosomes in genes with high R_{tc} values in aged D1 SPNs to genes with low R_{tc} values in aged D1 SPNs (top and bottom 15%). The average density of 3′ UTR ribosomes induced by PQ or siABCE1 was ~3- to 4-fold higher in high R_{tc} genes compared to low R_{tc} genes and was shifted significantly higher relative to control treatments (Figures 3D and 3E). These observations support our model, indicating that 3′ UTR ribosomes are induced under conditions that trigger 3′ UTR accumulation specifically in those genes, which exhibit aging-associated increases in R_{tc} values.

The bulk of ribosome-protected fragments recovered from our ribosome profiling assay were 27–31 nt long, corresponding to the region protected by an 80S ribosome. However, a small proportion (~0.5%–2.5%) of recovered fragments corresponded to a second peak at ~15 nt (Figure S3D). These short fragments have been shown to result from cleavage upstream of a stalled ribosome and subsequent protection by an upstream translating ribosome, which stalls when the A site of the ribosome reaches the cleavage site (Figure 3F; Guydosh and Green, 2014; Young et al., 2015). This stalled ribosome can in turn induce mRNA cleavage upstream, resulting in a chain reaction for hundreds of nucleotides upstream of the initial cleavage event and the enrichment of short ribosome-protected fragments throughout this region.

We quantified short cleavage fragments as a proportion of the total number of recovered ribosome-protected fragments (Figure 3F). *ABCE1* knockdown and PQ treatments increased the proportion of cleavage fragments by ~2- to 3-fold. A metagene plot of these short cleavage fragments centered at the stop codon exhibited a peak just upstream of the stop codon and extending ~200-nt upstream (Figure 3G). This pattern was also observed in a reanalysis of the shABCE1 (short hairpin RNA to ABCE1) knockdown in K562 cells (Figures S3E and S3F; Mills et al., 2016). Short cleavage fragments were enriched to the largest extent just upstream of the stop codon, whereas PQ and *ABCE1* knockdown increased the density of short cleavage fragments both upstream and downstream of the stop codon (Figure 3G, inset), consistent with the variability observed in the precise boundaries of 3′ UTR enrichment. Similar to full-length ribosome-protected fragments, short cleavage fragments were more enriched in response to PQ or *ABCE1* knockdown in the 3′ UTRs of high R_{tc} genes (Figure S3G). These results suggest that endonucleolytic transcript cleavage occurs frequently near stop codons and is increased under conditions of oxidative stress or direct depletion of *ABCE1* for a subset of mRNAs.

Endonucleolytically cleaved mRNAs are susceptible to degradation by 5′ terminal exonuclease (TEX) treatment because they are not protected at their 5′ ends by a cap. We isolated total RNA from the above cellular conditions and sequenced this material before and after TEX treatment. In untreated samples, we identified a subset of candidate induced 3′ UTR genes with increased R_{tc} relative to the control in both the *Abce1* knockdown and PQ conditions (Figure S3H). In the TEX-treated cells, however, no difference in R_{tc} was observed among control, PQ, and *Abce1* knockdown treatments, consistent with high R_{tc} values resulting from endonucleolytic cleavage.

Together, these observations provide support for our model in which age-associated oxidative stress and the subsequent impairment of the activity of the ribosome recycling factor ABCE1 triggers 3′ UTR ribosomes, mRNA cleavage in the vicinity of the stop codon, and, ultimately, the accumulation of isolated 3′ UTRs for many genes in the aging brain. However, the observed patterns are complex and other processes may contribute as well.

Isolated 3′ UTRs Accumulate in the Aging Human Brain and Vary Between Brain Regions

To determine whether isolated 3′ UTRs accumulate in the aging human brain, we analyzed RNA-seq data from various human cells and tissues from individuals of varying ages. An analysis of the total RNA sequencing data from immunopanned human astrocytes derived from 16 individuals (Zhang et al., 2016) identified dozens of genes with read coverages several-fold higher than their 3′ UTRs, with a pronounced increase in read density beginning at or just beyond the stop codon, as illustrated for *SOX9* (Figure 4A). Furthermore, the extent of 3′ UTR enrichment in *SOX9* increased with age (Figure 4A, inset; $p = 0.00016$, F-test). More broadly, an analysis of 1,380 poly(A)-selected RNA-seq samples representing 30 different tissues collected as part of the Genome-Tissue Expression (GTEx) project (GTEx Consortium, 2015) identified brain region- and age-specific patterns of 3′ UTR enrichment. The R_{tc} values among brain-derived tissues were positively associated with age, with a significantly increased slope compared to non-brain tissues (Figures 4B, S4A, and S4B; $p < 2.2e{-}16$, F-test). Under our model of isolated 3′ UTR biogenesis, reduced ABCE1 activity should be associated with higher levels of 3′ UTR enrichment. Consistent with this prediction, among the 320 GTEx human neuronal tissues, *ABCE1* expression was significantly lower in samples with higher mean R_{tc} (Figure 4C, $p = 1.7e{-}25$, F-test). *ABCE1* gene expression levels also declined significantly as a function of sample age (Figure S4C; $p = 2.9e{-}6$, F-test) but correlated more strongly with sample R_{tc} than with age.

Among the 12 different regions of the brain analyzed by the GTEx consortium, the slope of R_{tc} versus age was generally positive but exhibited significant variation ($p < 2.2e{-}16$, ANOVA), with only the cerebellum exhibiting a negative correlation with age (Figure 4D). These findings suggest that, although 3′ UTR enrichment is associated with increased age, this phenomenon is much more prevalent in neuronal than non-neuronal tissues, with different neuronal cell types exhibiting this phenomenon to different extents. In the aging brain, signatures of oxidative damage accumulate in more metabolically active brain regions (Corral-Debrinski et al., 1992). In particular, regional levels of aerobic glycolysis correlate spatially with amyloid-β deposition and are associated with increased levels of oxidative stress and susceptibility to neurodegenerative disease (Vlassenko et al., 2010). We noted that the regions of the brain with the highest and lowest basal rates of aerobic glycolysis (Goyal et al., 2017)—the frontal cortex and the cerebellum, respectively—exhibited the highest and lowest levels of age-associated 3′ UTR accumulation, respectively. These observations suggest that metabolic differences may contribute to brain region-specific differences in 3′ UTR accumulation.

Neuronal Isolated 3′ UTR Accumulation Correlates with Mitochondrial Gene Expression

The aging human brain is known to experience sustained exposure to ROS (Mattson and Magnus, 2006). We sought to determine whether signatures of increased oxidative stress were associated with increased 3′ UTR enrichment. To identify genes associated with isolated 3′ UTRs, we calculated the mean R_{tc} value across genes in each GTEx brain sample as a summary statistic. This vector of mean R_{tc} values was then correlated to the vector of gene expression values in matched samples, for every gene. The resulting correlations and p values were subsequently ranked to identify genes of interest (Figure 4E). Strikingly, 45 of the 100 genes most positively correlated with mean per sample R_{tc} across GTEx samples were core mitochondrial genes or

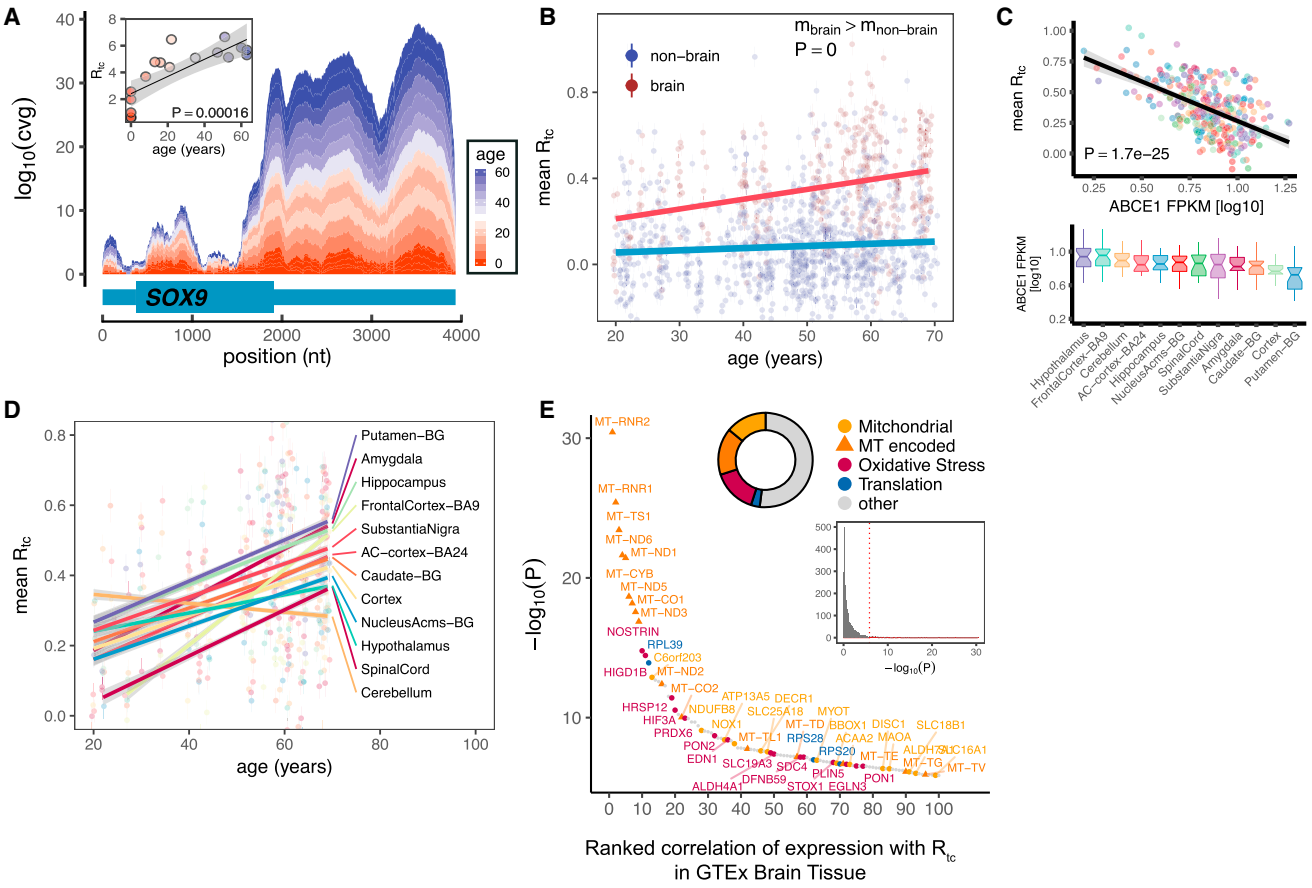

Figure 4. 3′ UTR-Enriched Genes Accumulate in the Aging Human Brain and Are Associated with Translation of Short Peptides

(A) Stacked plot of the $\log_{10}$ coverage of *Sox9* in human astrocytes colored by age. Inset is the R_{tc} value plotted as a function of age (p value by F-test).

(B) The relationship between age and the mean R_{tc} in 1380 GTEx samples colored by brain and non-brain tissues and the linear fit between age and R_{tc} across all genes for brain and non-brain tissues. For each individual sample, the mean R_{tc} and confidence intervals about the mean are plotted versus age.

(C) The mean R_{tc} in neuronal GTEx samples plotted against expression of ABCE1 and boxplots of the distribution of *ABCE1* gene expression in different neuronal tissues. Samples with decreased ABCE1 levels exhibit significantly higher average R_{tc} (p value by F-test).

(D) The relationship between age and R_{tc} separated by brain region.

(E) The top 100 genes most positively correlated with increased R_{tc} in neuronal GTEx samples by rank and p value. Insets are a donut plot demonstrating the distribution of functional classifications of genes and a histogram of the p value distribution of positive gene correlations.

oxidative stress response genes, including 16 mitochondrial-encoded transcripts. Applying the same approach to RNA-seq data from cultured mouse cortical neurons treated with a panel of drugs (Figure S4D), we again observed that mitochondrial genes were among the most strongly correlated with increased R_{tc} (Figure S4E). In both of these analyses, although mitochondrial genes encoded on both the nuclear and mitochondrial genomes were robustly enriched, mitochondrial-encoded transcripts ranked most highly. These results confirm an association between 3′ UTR enrichment and upregulation of mitochondrial genes and oxidative stress response genes in both humans and mice.

Evidence that 3′ UTR-Encoded Peptides Originate from Isolated 3′ UTR Genes

In both human and mouse, some 3′ UTR sequences accumulate more than others (Figure 1F and 4B). By examining the 3′ UTR sequences of high R_{tc} genes, we observed that genes with higher R_{tc} were most likely to have TGA stop codons and least likely to have TAA (Figures S5A and S5B; $p < 1e{-}10$, D1 SPNs; $p = 0.0043$, GTEx, Cochrane-Armitage Test). A stop codon sequence can influence the fidelity of termination (Dabrowski et al., 2015) and may contribute to gene-specific differences in isolated 3′ UTR accumulation. We also observed that the median distance from the canonical stop codon to the first 3′ UTR stop codon (in any frame) was ~2-fold longer for genes with higher 3′ UTR enrichment in both humans and mice (but still much shorter than the main ORF) (Figure 5A). This observation raised the possibility that 3′ UTR ribosomes may be actively translating in some cases. In yeast, 3′ UTR-encoded peptides are produced when the *ABCE1* homolog *Rli1* is inhibited (Young et al., 2015).

To explore the possibility that peptides are produced from ribosomes associated with isolated 3′ UTRs in mammals, we analyzed tandem mass-spectrometry (MS/MS) data derived from post-mortem human brain surveyed across 7 different tissues (Carlyle et al., 2017). Spectra were mapped to both the UniProt protein database as well as a custom database of translated

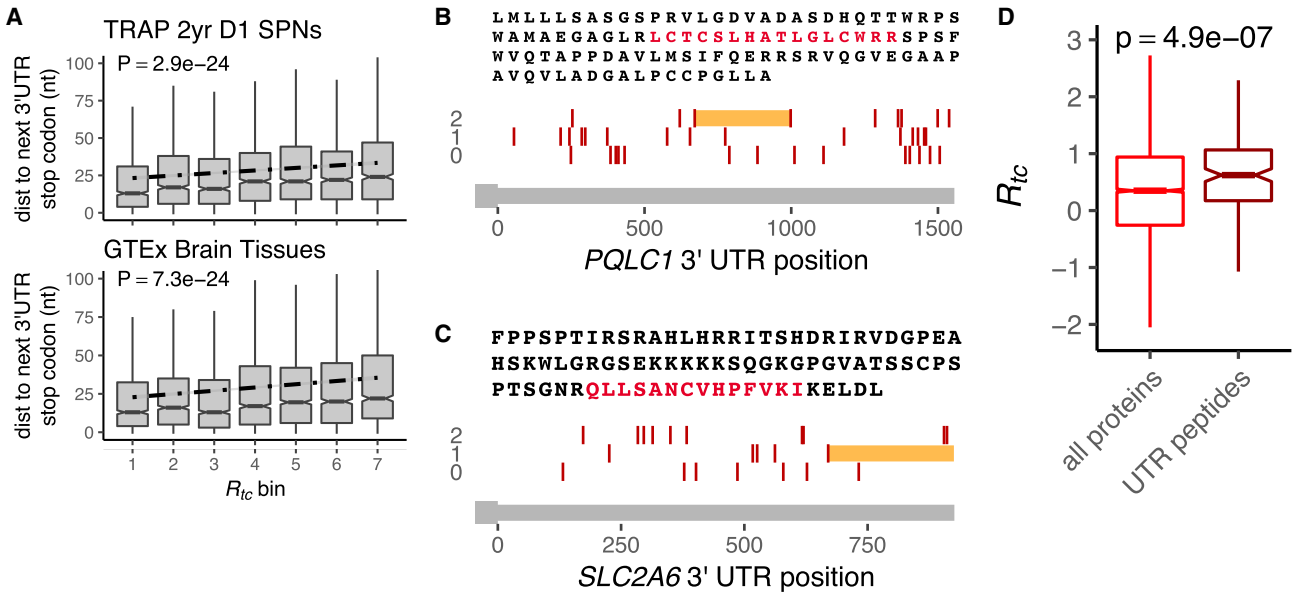

Figure 5. Evidence of 3′ UTR-Encoded Peptides Originating from Isolated 3′ UTR Genes

(A) Box plots of the distribution of distances from the stop codon to the next 3′ UTR stop codon (in any frame) plotted as a function of R_{tc} in 7 equal sized bins.

(B) Example of translated 3′ UTR ORFs from the 3′ UTRs of *PQLC1* and (c) *SLC2A6*. Red vertical dashes indicate stop codons in frames relative to the canonical stop codon. Red text indicates the peptide spectra that mapped to the 3′ ORF, which is shown in orange.

(C) Example of translated 3′ UTR ORFs from the 3′ UTRs of *SLC2A6*. Red vertical dashes indicate stop codons in frames relative to the canonical stop codon. Red text indicates the peptide spectra that mapped to the 3′ ORF, which is shown in orange.

(D) Box plots of the mean R_{tc} for all genes compared to those with 3′ UTR peptides (p = 4.9e−7, t test).

3′ UTR ORFs (STAR Methods). As a positive control for our computational pipeline, we detected an average of 9,648 high-confidence annotated proteins per sample, consistent with previous analyses. We also detected 470 high-confidence 3′ UTR ORF-derived peptides (at a false discovery rate of 0.01), which were on average 52 amino acids long and lacked recognizable protein domains (e.g., see Figures 5B, 5C, and S5C). Genes with associated 3′ UTR peptides had significantly higher R_{tc} values compared to similarly expressed genes whose annotated proteins were detected by mass spectrometry (Figure 5D, p = 4.9e−7, t test), suggesting that these peptides may be produced from isolated 3′ UTRs or that the production of isolated 3′ UTRs and 3′ UTR-encoded peptides involves related mechanisms. These peptides were derived from all three ORFs relative to the upstream canonical ORF in similar proportions (Figure S5D). Thus, the active translation of isolated 3′ UTRs may be a biological consequence of increased oxidative stress, but whether the resulting peptides have function is not clear.

DISCUSSION

Here, we have documented the widespread accumulation of isolated 3′ UTR RNA species, observed several times previously, and we demonstrate an association with age and present a model for their biogenesis (Figure 3A). Although other mechanisms may also contribute to isolated 3′ formation, our model proposes that a consequence of age-associated oxidative stress is the impairment of the ribosome-recycling factor ABCE1 and endonucleolytic cleavage near stop codon-arrested ribosomes. Four main lines of evidence support our proposed mechanism. First, isolated 3′ UTRs are consistently associated with, and can be directly induced by, oxidative stress. Second, impairment of the ribosome recycling factor ABCE1, which occurs under conditions of oxidative stress, induces 3′ UTR accumulation. Third, inhibition of ABCE1 either directly or by oxidative stress increases the abundance of 3′ UTR ribosomes specifically in those genes that exhibit isolated 3′ UTR production. Finally, inhibition of ABCE1 directly or by oxidative stress increases the proportion of short cleavage-associated ribosome-protected fragments at and around the stop codon, providing direct evidence that isolated 3′ UTRs are produced by cleavage of larger RNAs. Thus, the transcriptome may be reshaped by No-Go decay under stress.

Isolated 3′ UTRs appear to be a cell-type- and region-specific biomarker of neuronal aging and oxidative stress. Although specific functions are not known, the broad scale of this phenomenon is likely to contribute to one or more biologically important processes. Because the production of isolated 3′ UTRs is presumably accompanied by degradation of the coding portion of the message, downregulation of the expression of the associated proteins is likely, as has been observed previously (Kocabas et al., 2015). This downregulation likely has a variety of biological consequences, independent of any role of the isolated 3′ UTR species. Furthermore, the accumulation of 3′ UTRs could itself have significant impact. mRNA 3′ UTRs play many roles in the cell, regulating mRNA localization, stability, and translation via regulatory elements (Kuersten and Goodwin, 2003). The presence of excess 3′ UTR sequences in the cell could thus sequester RNA-binding proteins or microRNAs, analogous to some circular RNAs or to

CUG repeat RNAs in myotonic dystrophy (Goodwin et al., 2015; Hansen et al., 2013). The 3′ UTR may also have a scaffolding function, directing protein-protein interactions (Berkovits and Mayr, 2015), and free 3′ UTRs might perturb these functions.

The physical association between isolated 3′ UTRs and ribosomes suggests additional potential functions. For example, isolated 3′ UTRs may globally reduce translation efficiency by sequestering large numbers of ribosomes. Additionally, 3′ UTR-derived peptides might have cellular consequences. A recent study identified short peptides generated from upstream ORFs (uORFs) during the integrated stress response that were predicted to have high affinity for major histocompatibility class I antigens of the adaptive immune system (Starck et al., 2016). Peptides generated from 3′ UTRs in the aging brain could similarly elicit immune responses, contributing to age-associated inflammation, or could contribute to the formation of protein aggregates or other proteotoxic stresses commonly observed in aging brains.

The relationship between aging and isolated 3′ UTRs has inclined us toward potential detrimental consequences of 3′ UTR accumulation. However, it is also possible that isolated 3′ UTRs contribute to adaptive cellular responses. In *Salmonella*, endonucleolytic cleavage of the *cpxP* 3′ UTR produces a small RNA that mediates a protective response against inner membrane damage (Chao and Vogel, 2016). Various types of cellular stress trigger global shifts in translation. In yeast, formation of the prion [PSI^+] form of the termination factor protein Sup35p promotes read-through of nonsense codons, providing a survival advantage under various conditions (True et al., 2004). Analogously, the induction of 3′ UTR translation under oxidative stress in aging or neurodegenerative disease might contribute in some way to the stress response.

STAR★METHODS

Detailed methods are provided in the online version of this paper and include the following:

- KEY RESOURCES TABLE
- CONTACT FOR REAGENT AND RESOURCE SHARING
- EXPERIMENTAL MODEL AND SUBJECT DETAILS
  - Mouse models
  - Cell Lines
- METHOD DETAILS
  - TRAP profiling
  - Datasets
  - RNaseq / TRAPseq read mapping and expression quantification
  - Calculation of R_{tc}
  - Meta analyses
  - Genes correlated with R_{tc}
  - Sequence Logos
  - Lipofuscin quantification
  - Western Blotting
  - Ribosome Profiling
  - TEX Treatment
  - Analysis of proteomic data
- QUANTIFICATION AND STATISTICAL ANALYSIS
- DATA AND SOFWARE AVAILABILITY

SUPPLEMENTAL INFORMATION

Supplemental Information includes five figures and four tables and can be found with this article online at https://doi.org/10.1016/j.celrep.2018.10.094.

ACKNOWLEDGMENTS

We thank Phil Sharp, Torben Jensen, Søren Lykke-Andersen, Wendy Gilbert, Marcus E. Raichle, Manu S. Goyal, and members of the Burge lab for comments on the manuscript and Hiten Madhani for helpful suggestions regarding iron-sulfur cluster proteins. P.H.S. was supported by a Genentech Life Sciences Research Fellowship, and H.L. was supported by a postdoctoral fellowship from the JPB Foundation. This work was supported by an award from the JPB Foundation (M.H.) and by NIH grant number HG002439 (to C.B.B.).

AUTHOR CONTRIBUTIONS

P.H.S. performed experiments, analyses, and drafted the manuscript. H.L. performed mouse microscopy and additional experiments. D.D. contributed to experiments. M.S.G. and M.E.R. contributed PET experimental data and analysis of brain metabolism. M.H. supervised the project, performed TRAP experiments, and revised the manuscript. C.B.B. supervised the project and revised the manuscript. All authors reviewed and approved the final manuscript.

DECLARATION OF INTERESTS

The authors declare no competing interests.

Received: June 26, 2017
Revised: September 24, 2018
Accepted: October 25, 2018
Published: November 27, 2018

REFERENCES

Alhebshi, A., Sideri, T.C., Holland, S.L., and Avery, S.V. (2012). The essential iron-sulfur protein Rli1 is an important target accounting for inhibition of cell growth by reactive oxygen species. Mol. Biol. Cell *23*, 3582–3590.

Arribere, J.A., and Fire, A.Z. (2018). Nonsense mRNA suppression via nonstop decay. eLife *7*, 1470.

Berkovits, B.D., and Mayr, C. (2015). Alternative 3′ UTRs act as scaffolds to regulate membrane protein localization. Nature *522*, 363–367.

Brumaghim, J.L., Li, Y., Henle, E., and Linn, S. (2003). Effects of hydrogen peroxide upon nicotinamide nucleotide metabolism in Escherichia coli: changes in enzyme levels and nicotinamide nucleotide pools and studies of the oxidation of NAD(P)H by Fe(III). J. Biol. Chem. *278*, 42495–42504.

Carlyle, B.C., Kitchen, R.R., Kanyo, J.E., Voss, E.Z., Pletikos, M., Sousa, A.M.M., Lam, T.T., Gerstein, M.B., Šestan, N., and Nairn, A.C. (2017). A multiregional proteomic survey of the postnatal human brain. Nat. Neurosci. *20*, 1787–1795.

Carninci, P., Sandelin, A., Lenhard, B., Katayama, S., Shimokawa, K., Ponjavic, J., Semple, C.A.M., Taylor, M.S., Engström, P.G., Frith, M.C., et al. (2006). Genome-wide analysis of mammalian promoter architecture and evolution. Nat. Genet. *38*, 626–635.

Carpenter, A.E., Jones, T.R., Lamprecht, M.R., Clarke, C., Kang, I.H., Friman, O., Guertin, D.A., Chang, J.H., Lindquist, R.A., Moffat, J., et al. (2006). CellProfiler: image analysis software for identifying and quantifying cell phenotypes. Genome Biol. *7*, R100.

Chao, Y., and Vogel, J. (2016). A 3′ UTR-derived small RNA provides the regulatory noncoding arm of the inner membrane stress response. Mol. Cell *61*, 352–363.

Corral-Debrinski, M., Horton, T., Lott, M.T., Shoffner, J.M., Beal, M.F., and Wallace, D.C. (1992). Mitochondrial DNA deletions in human brain: regional variability and increase with advanced age. Nat. Genet. *2*, 324–329.

Dabrowski, M., Bukowy-Bieryllo, Z., and Zietkiewicz, E. (2015). Translational readthrough potential of natural termination codons in eucaryotes–The impact of RNA sequence. RNA Biol. *12*, 950–958.

Dobin, A., Davis, C.A., Schlesinger, F., Drenkow, J., Zaleski, C., Jha, S., Batut, P., Chaisson, M., and Gingeras, T.R. (2013). STAR: ultrafast universal RNA-seq aligner. Bioinformatics *29*, 15–21.

Doma, M.K., and Parker, R. (2006). Endonucleolytic cleavage of eukaryotic mRNAs with stalls in translation elongation. Nature *440*, 561–564.

Fejes-Toth, K., Sotirova, V., Sachidanandam, R., and Assaf, G. (2009). Post-transcriptional processing generates a diversity of 5′-modified long and short RNAs. Nature *457*, 1028–1032.

Garneau, N.L., Wilusz, J., and Wilusz, C.J. (2007). The highways and byways of mRNA decay. Nat. Rev. Mol. Cell Biol. *8*, 113–126.

Gerashchenko, M.V., and Lobanov, A.V. (2012). Genome-wide ribosome profiling reveals complex translational regulation in response to oxidative stress. Proc. Natl. Acad. Sci. USA *109*, 17394–17399.

Gokce, O., Stanley, G.M., Treutlein, B., Neff, N.F., Camp, J.G., Malenka, R.C., Rothwell, P.E., Fuccillo, M.V., Südhof, T.C., and Quake, S.R. (2016). cellular taxonomy of the mouse striatum as revealed by single-cell RNA-seq. Cell Rep. *16*, 1126–1137.

Goodwin, M., Mohan, A., Batra, R., Lee, K.-Y., Charizanis, K., Fernández Gómez, F.J., Eddarkaoui, S., Sergeant, N., Buée, L., Kimura, T., et al. (2015). MBNL sequestration by toxic RNAs and RNA misprocessing in the myotonic dystrophy brain. Cell Rep. *12*, 1159–1168.

Goyal, M.S., Vlassenko, A.G., Blazey, T.M., Su, Y., Couture, L.E., Durbin, T.J., Bateman, R.J., Benzinger, T.L.-S., Morris, J.C., and Raichle, M.E. (2017). Loss of brain aerobic glycolysis in normal human aging. Cell Metab. *26*, 353–360.e3.

GTEx Consortium (2015). Human genomics. The Genotype-Tissue Expression (GTEx) pilot analysis: multitissue gene regulation in humans. Science *348*, 648–660.

Guydosh, N.R., and Green, R. (2014). Dom34 rescues ribosomes in 3′ untranslated regions. Cell *156*, 950–962.

Hansen, T.B., Jensen, T.I., Clausen, B.H., Bramsen, J.B., Finsen, B., Damgaard, C.K., and Kjems, J. (2013). Natural RNA circles function as efficient microRNA sponges. Nature *495*, 384–388.

Heiman, M., Schaefer, A., Gong, S., Peterson, J.D., Day, M., Ramsey, K.E., Suárez-Fariñas, M., Schwarz, C., Stephan, D.A., Surmeier, D.J., et al. (2008). A translational profiling approach for the molecular characterization of CNS cell types. Cell *135*, 738–748.

Heiman, M., Kulicke, R., Fenster, R.J., Greengard, P., and Heintz, N. (2014). Cell type-specific mRNA purification by translating ribosome affinity purification (TRAP). Nat. Protoc. *9*, 1282–1291.

Hornstein, N., Torres, D., Das Sharma, S., Tang, G., Canoll, P., and Sims, P.A. (2016). Ligation-free ribosome profiling of cell type-specific translation in the brain. Genome Biol. *17*, 149.

Ibrahim, F., Maragkakis, M., Alexiou, P., and Mourelatos, Z. (2018). Ribothrypsis, a novel process of canonical mRNA decay, mediates ribosome-phased mRNA endonucleolysis. Nat. Struct. Mol. Biol. *25*, 302–310.

Karginov, F.V., Cheloufi, S., Chong, M.M.W., Stark, A., Smith, A.D., and Hannon, G.J. (2010). Diverse endonucleolytic cleavage sites in the mammalian transcriptome depend upon microRNAs, Drosha, and additional nucleases. Mol. Cell *38*, 781–788.

Kocabas, A., Duarte, T., Kumar, S., and Hynes, M.A. (2015). Widespread differential expression of coding region and 3′ UTR sequences in neurons and other tissues. Neuron *88*, 1149–1156.

Kuersten, S., and Goodwin, E.B. (2003). The power of the 3′ UTR: translational control and development. Nat. Rev. Genet. *4*, 626–637.

Leng, N., Dawson, J.A., Thomson, J.A., Ruotti, V., Rissman, A.I., Smits, B.M.G., Haag, J.D., Gould, M.N., Stewart, R.M., and Kendziorski, C. (2013). EBSeq: an empirical Bayes hierarchical model for inference in RNA-seq experiments. Bioinformatics *29*, 1035–1043.

Li, B., and Dewey, C.N. (2011). RSEM: accurate transcript quantification from RNA-seq data with or without a reference genome. BMC Bioinformatics *12*, 323.

López-Otín, C., Blasco, M.A., Partridge, L., Serrano, M., and Kroemer, G. (2013). The hallmarks of aging. Cell *153*, 1194–1217.

Malka, Y., Steiman-Shimony, A., Rosenthal, E., Argaman, L., Cohen-Daniel, L., Arbib, E., Margalit, H., Kaplan, T., and Berger, M. (2017). Post-transcriptional 3′-UTR cleavage of mRNA transcripts generates thousands of stable uncapped autonomous RNA fragments. Nat. Commun. *8*, 2029.

Martin, M. (2011). Cutadapt removes adapter sequences from high-throughput sequencing reads. EMBnet.Journal *17*. https://doi.org/10.14806/ej.17.1.200.

Mattson, M.P., and Magnus, T. (2006). Ageing and neuronal vulnerability. Nat. Rev. Neurosci. *7*, 278–294.

McIlwain, S., Tamura, K., Kertesz-Farkas, A., Grant, C.E., Diament, B., Frewen, B., Howbert, J.J., Hoopmann, M.R., Käll, L., Eng, J.K., et al. (2014). Crux: rapid open source protein tandem mass spectrometry analysis. J. Proteome Res. *13*, 4488–4491.

Mercer, T.R., Wilhelm, D., Dinger, M.E., Soldà, G., Korbie, D.J., Glazov, E.A., Truong, V., Schwenke, M., Simons, C., Matthaei, K.I., et al. (2011). Expression of distinct RNAs from 3′ untranslated regions. Nucleic Acids Res. *39*, 2393–2403.

Mills, E.W., Wangen, J., Green, R., and Ingolia, N.T. (2016). Dynamic regulation of a ribosome rescue pathway in erythroid cells and platelets. Cell Rep. *17*, 1–10.

Nandy, K. (1971). Properties of neuronal lipofuscin pigment in mice. Acta Neuropathol. *19*, 25–32.

Puig, S., Askeland, E., and Thiele, D.J. (2005). Coordinated remodeling of cellular metabolism during iron deficiency through targeted mRNA degradation. Cell *120*, 99–110.

Starck, S.R., Tsai, J.C., Chen, K., Shodiya, M., Wang, L., Yahiro, K., Martins-Green, M., Shastri, N., and Walter, P. (2016). Translation from the 5′ untranslated region shapes the integrated stress response. Science *351*, aad3867.

True, H.L., Berlin, I., and Lindquist, S.L. (2004). Epigenetic regulation of translation reveals hidden genetic variation to produce complex traits. Nature *431*, 184–187.

Tsuboi, T., Kuroha, K., Kudo, K., Makino, S., Inoue, E., Kashima, I., and Inada, T. (2012). Dom34:Hbs1 plays a general role in quality-control systems by dissociation of a stalled ribosome at the 3′ end of aberrant mRNA. Mol. Cell *46*, 518–529.

Veatch, J.R., McMurray, M.A., Nelson, Z.W., and Gottschling, D.E. (2009). Mitochondrial dysfunction leads to nuclear genome instability via an iron-sulfur cluster defect. Cell *137*, 1247–1258.

Vlassenko, A.G., Vaishnavi, S.N., Couture, L., Sacco, D., Shannon, B.J., Mach, R.H., Morris, J.C., Raichle, M.E., and Mintun, M.A. (2010). Spatial correlation between brain aerobic glycolysis and amyloid-β (Aβ) deposition. Proc. Natl. Acad. Sci. USA *107*, 17763–17767.

Wu, X., and Bartel, D.P. (2017). kpLogo: positional k-mer analysis reveals hidden specificity in biological sequences. Nucleic Acids Res. *45* (*W1*), W534–W538.

Young, D.J., Guydosh, N.R., Zhang, F., Hinnebusch, A.G., and Green, R. (2015). Rli1/ABCE1 recycles terminating ribosomes and controls translation reinitiation in 3'UTRs in vivo. Cell *162*, 872–884.

Zhang, X.O., Wang, H.B., Zhang, Y., Lu, X., Chen, L.L., and Yang, L. (2014). Complementary sequence-mediated exon circularization. Cell *159*, 134–147.

Zhang, Y., Sloan, S.A., Clarke, L.E., Caneda, C., Plaza, C.A., Blumenthal, P.D., Vogel, H., Steinberg, G.K., Edwards, M.S.B., Li, G., et al. (2016). Purification and characterization of progenitor and mature human astrocytes reveals transcriptional and functional differences with mouse. Neuron *89*, 37–53.

Zou, X., Ratti, B.A., O'Brien, J.G., Lautenschlager, S.O., Gius, D.R., Bonini, M.G., and Zhu, Y. (2017). Manganese superoxide dismutase (SOD2): is there a center in the universe of mitochondrial redox signaling? J. Bioenerg. Biomembr. *49*, 325–333.

STAR★METHODS

KEY RESOURCES TABLE

REAGENT or RESOURCE	SOURCE	IDENTIFIER
Antibodies		
Rabbit monoclonal anti-ABCE1	Abcam	ab185548
Rabbit polyclonal anti-Histone H3	Abcam	ab1791; RRID: AB_302613
Rabbit polyclonal anti-GFP	Abcam	ab6556; RRID: AB_305564
Rabbit monoclonal anti-EXOSC3	Abcam	ab190689
Mouse monoclonal anti-β-actin	Sigma	A5441; RRID: AB_476744
Biological Samples		
DMEM	ThermoFisher	11965-092
Opti-MEM	ThermoFisher	31985-092
FBS	Hyclone	SH30071.03
Human Origene TissueScan cDNA	Origene	Hbrt101
Mouse Origene TissueScan cDNA	Origene	Mdrt101
Chemicals, Peptides, and Recombinant Proteins		
Lipofectamine RNAiMAX	ThermoFisher	13778150
phosphatase inhibitor cocktail	ThermoFisher	78441
BCA	ThermoFisher	23227
ECL Plus	ThermoFisher	32132
Critical Commercial Assays		
QIAGEN RNeasy spin columns	QIAGEN	74106
On-column DNase Digestion	QIAGEN	79254
Hi Capacity cDNA kit	ThermoFisher	4368813
KAPA Sybr Master Mix	Kapa Biosystems	KK4618
TaqMan Gene Expression Master Mix	ThermoFisher	4369514
Deposited Data		
TRAP sequencing of young and aged D1 and D2 SPNs	GEO	GSE97461
Ribosome Profiling under different conditions	GEO	GSE97461
Experimental Models: Cell Lines		
NIH 3T3 cell line	ATCC	Cat# CRL-6442
Experimental Models: Organisms/Strains		
Drd1::EGFP-L10a (C56BL/6J background)	Laboratory of M. Heiman	*Drd1::EGFP-L10a*
Drd2::EGFP-L10a (C56BL/6J background)	Laboratory of M. Heiman	*Drd2::EGFP-L10a*
Oligonucleotides		
See Table S2	This Study	N/A
Sequence-Based Reagents		
Silencer Select pre-designed siRNA Abce1 siRNA	ThermoFisher	s76800
Silencer Select pre-designed siRNA negative control siRNA	ThermoFisher	4390844
Silencer Select pre-designed siRNA Exosc3 siRNA	ThermoFisher	s83101
TaqMan Human ABCE1 primer	ThermoFisher	Hs01003006_g1 FAM-MGB
TaqMan Human ACTB primer	ThermoFisher	Hs01060655_g1 VIC-MGB-PL
TaqMan Mouse Abce1 primer	ThermoFisher	Mm00649858_m1 FAM-MGB
TaqMan Mouse Actb primer	ThermoFisher	Mm00607939_s1 VIC-MGB-PL

(*Continued on next page*)

Continued

REAGENT or RESOURCE	SOURCE	IDENTIFIER
Software and Algorithms		
STAR version 2.5.1b	(Dobin et al., 2013)	https://github.com/alexdobin/STAR
EBSeq version 1.1.5	(Leng et al., 2013)	https://bioconductor.org/packages/release/bioc/html/EBSeq.html
RSEM 1.2.20	(Li and Dewey, 2011)	https://deweylab.github.io/RSEM/
CIRCexplorer 1.1.10	(Zhang et al., 2014)	https://github.com/YangLab/CIRCexplorer
CellProfiler	(Carpenter et al., 2006)	http://cellprofiler.org
FASTX toolkit 0.0.14		http://hannonlab.cshl.edu/fastx_toolkit/index.html
Cutadapt version 1.14	(Martin, 2011)	http://cutadapt.readthedocs.io/en/stable/installation.html
Other		
RNA Sequencing Datasets Assessed – See Table S1	N/A	N/A

CONTACT FOR REAGENT AND RESOURCE SHARING

Further information and requests for resources and reagents should be directed to and will be fulfilled by the Lead Contact, Christopher Burge (cburge@mit.edu).

EXPERIMENTAL MODEL AND SUBJECT DETAILS

All mouse experiments were conducted with the approval and oversight of the MIT Animal Care and Use Committee.

Mouse models

Female BAC transgenic mouse lines *Drd1::EGFP-L10a* and *Drd2::EGFP-L10a* on a C56BL/6J background at 6 weeks of age (PN42) and 2-years of age were used for experiments. Mice were decapitated and brain tissue was immediately dissected and used for TRAP RNA purification as described in Heiman et al., 2008 (Heiman et al., 2008).

Cell Lines

NIH 3T3 cells were grown at 37°C at 5% CO_2 in DMEM supplemented with 10% FBS and 1% penicillin/streptomycin. Knockdowns were performed with Silencer Select pre-designed siRNAs. Transfection was performed with Lipofectamine RNAiMAX Reagent in Opti-MEM as per manufactures instructions with 75pmol of siRNA per well of a 6-well cell-culture dish for *ABCE1* knockdown and 400pmol for *EXOSC3* knockdown.

METHOD DETAILS

TRAP profiling

Immediately following decapitation, TRAP profiling was performed as detailed in Heiman et al., 2014 (Heiman et al., 2014). RNA-seq libraries were prepped using NuGEN Ovation V2.0 system.

Datasets

Datasets assessed in this study and associated accession numbers and PubMed IDs if available are listed in Table S1.

RNaseq / TRAPseq read mapping and expression quantification

Reads were mapped to the mouse or human genomes version GRCm38/mm10 or GRCh37/hg19 respectively using the STAR read aligner version 2.5.1b (Dobin et al., 2013) with ENSEMBL Version 75 gene annotations to guide exon-exon junction alignment. Gene expression values were quantified using RSEM version 1.2.20 (Li and Dewey, 2011) and differences in gene expression between experimental conditions were estimated using EBSeq version 1.1.5 (Leng et al., 2013) again using ENSEMBL Version 75 annotations. To identify junction reads, which might indicate the presence of circular RNAs, we used the chimeric/fusion alignment functionality of STAR. Reads were mapped using standard parameters in addition to: *"–chimSegmentMin 15–chimJunctionOverhangMin 15."* The CIRCexplorer tool was then used to quantify circular RNAs from these alignments (Zhang et al., 2014).

Calculation of R_{tc}

$R_{tc,}$ or the "termination codon ratio," was defined as the log base 2 of the ratio of the mean read coverage after the annotated stop codon to the mean read coverage before the annotated stop codon:

$$R_{tc} = log_2 \left(\frac{\frac{1}{l - tc} \sum_{i=tc}^{i=l} cvg(i)}{\frac{1}{tc - 1} \sum_{k=0}^{k=tc-1} cvg(k)} \right)$$

assuming a gene of length *l* with an annotated stop codon at *tc*. A minimum value of 1 was used for numerator and denominator to avoid division by zero. Only constitutive exons were included in the calculation and overlapping genes and genes with multiple annotated protein coding stop codons were excluded from analyses. Negative R_{tc} values occur when the mean 3′ UTR coverage is less than the mean gene body coverage, since log(x) < 0 when x < 1. We have found that for some library preparations sequence coverage over the 3′ UTR is, on average, lower than that over the gene body across most genes, leading to negative R_{tc} values. In general, because of the potential for such biases, R_{tc} can be compared only between different experimental conditions or treatments for which library preparation and sequencing did not vary. When assayed by qRT-PCR, genes with high R_{tc} values generally had 3′ UTR expression that was severalfold higher than the associated CDS, indicating that CDS-containing transcripts from these loci are typically reduced but not absent.

Meta analyses

Meta-analysis plots of gene RNA-seq or ribosome profiling coverage were performed using constitutive exons of non-overlapping genes and excluded genes with multiple annotated protein coding stop codons. To plot the heatmap, coverage upstream and downstream of the stop codon (the 5′ UTR + ORF, and the 3′ UTR respectively), were normalized to windows of 1000 bins each. The minimum window coverage per transcript was subtracted from all windows and the result was normalized to sum to 1, log transformed, and smoothed using a Gaussian kernel 100 windows wide using the *smth* function of the R smoother package.

Genes correlated with R_{tc}

To identify genes with expression patterns correlated with R_{tc}, we first quantified the mean per-sample R_{tc}. We then computed the Pearson correlation of this vector with the vector of gene expression values for each of 18745 nuclear protein-coding genes supplemented with all genes encoded on the mitochondrial chromosome. The distribution of P values is plotted in Figure S4E. We then ranked the 3938 positively correlated genes by their Pearson correlation coefficients to identify genes expression patterns that accompanied increased R_{tc}.

Sequence Logos

Sequence logos in Figure S5A were generated with kpLogo (Wu and Bartel, 2017) from stop codon centered kmers ranked by R_{tc}.

Lipofuscin quantification

Male mice aged 9 weeks or 19 months from the *Drd1::EGFP-L10a* or *Drd2::EGFP-L10a* Bacterial Artificial Chromosome (BAC) transgenic lines (n = 3 each group) were used for lipofuscin measurements. Mouse brain tissue was perfused, embedded, fixed with 4% paraformaldehyde and cryosectioned at 20 μm thickness. Drd1 or Drd2 neurons expressing EGFP-L10a were stained with anti-GFP antibody (Abcam ab6556 1:5,000 dilution). Autofluorescent lipofuscin was visualized in both red and far-red channel. Zeiss LSM700 Confocal Microscope with a 40X objective lens was used. The percentage of Drd1 or Drd2 neurons containing lipofuscin was obtained by an examination of three tissue sections per mouse where two striatal images were taken in each tissue section. The proportion of lipofuscin per cell was quantified using CellProfiler (Carpenter et al., 2006).

Western Blotting

Cells were lysed with 1% SDS in water containing protease and phosphatase inhibitor cocktail (ThermoFisher). Protein concentration was measured with BCA (ThermoFisher) and loaded at 20 μg per lane. After electrophoresis, the proteins were transferred semi-dry to PVDF membrane. The membrane was incubated with 5% milk in PBS-T (PBS with 0.05% Tween20) for one hour at room temperature then incubated with following antibodies for over-night at 4°C: Abce1 (Abcam ab185548, 1:1000 dilution), Exosc3 (Abcam ab190689, 1:1000 dilution), Histone H3 (Abcam ab1791, 1:20,000 dilution). The following day, the membrane was washed three-times with PBS-T for 10 minutes each, incubated with a HRP-conjugated anti-rabbit secondary antibody for one hour at room temperature (1:10,000 dilution in PBS-T), washed three times, and developed with ECL Plus (ThermoFisher).

Ribosome Profiling

Ribosome profiling was performed using the Illumina TruSeq Ribo Profile kit (RPHMR12126) according to manufacturer's specifications with the following exceptions. Footprints spanning 15-32nt were excised from the RNA gel to capture both short and long ribosome protected fragments. Following end repair of size selected RNA fragments, sequencing libraries were prepped using the Clontech SMARTer smRNA-Seq kit (635030) as described in Hornstein et al. (Hornstein et al., 2016). Libraries were multiplex

sequenced on an Illumina NextSeq and the resulting demultiplexed sequences were collapsed to unique reads using fastx_collapser and trimmed of the polyA tails, template switching nucleotides, and adaptor sequences added by the SMARTer smRNA-Seq protocol using cutadapt.

TEX Treatment

TEX treatments were performed as described in Malka et al. (Malka et al., 2017).

Analysis of proteomic data

Mass spectrometry data for PXD001250 were downloaded from the PRIDE archive and RAW files were converted to mzML using MSconvert from the proteowizard package (http://proteowizard.sourceforge.net/). A custom peptide database was constructed by translating all 3′ UTR open reading frames 18 amino acids or longer. This database was combined with the UniProt SwissProt and trEMBL databases. The CRUX (McIlwain et al., 2014) mass spectrometry analysis toolkit was used to perform all subsequent searching, ranking and quantification of proteins and peptides and to construct a decoy database of peptides to empirically calculate a false discovery rate. The decoy database was constructed using the CRUX amino acid permutation method. Peptides were searched against our custom database and the decoy database using comet allowing for fixed carbamidomethylation modifications and variable N-acetylation and methionine oxidation. Percolator was then used to rank and score proteins using default options in addition to "–protein T" to perform fido protein scoring and ranking. A q-value threshold of 0.01 was used to filter the resulting proteins/peptides. Only 3′ UTR peptides that could be unambiguously assigned to having originated from the 3′ UTR, and not canonical ORFs, were considered in downstream analysis.

QUANTIFICATION AND STATISTICAL ANALYSIS

Statistical parameters and specific tests are reported in the text and figures including the statistical significance. Significance was defined as $p < 0.01$. All statistical test were performed using the R programming language. No statistical methods were employed *a-priori* for randomization, stratification, sample size estimation, or exclusion of any samples.

DATA AND SOFWARE AVAILABILITY

Sequencing datasets generated in this study have been deposited under accession number GEO: GSE97461. All software used in this manuscript is referenced in the methods. All custom code and pipelines are available upon request.